FLORE
Repository istituzionale dell'Università degli Studi di Firenze

ArcSAR: Theory, Simulations, and Experimental Verification

Questa è la Versione finale referata (Post print/Accepted manuscript) della seguente pubblicazione:

Original Citation:

ArcSAR: Theory, Simulations, and Experimental Verification / Pieraccini, Massimiliano; Miccinesi, Lapo. - In: IEEE TRANSACTIONS ON MICROWAVE THEORY AND TECHNIQUES. - ISSN 0018-9480. - ELETTRONICO. - 65:(2017), pp. 293-301. [10.1109/TMTT.2016.2613926]

Availability:

This version is available at: 2158/1059110 since: 2017-06-20T08:42:00Z

Published version:

DOI: 10.1109/TMTT.2016.2613926

Terms of use:

Open Access

La pubblicazione è resa disponibile sotto le norme e i termini della licenza di deposito, secondo quanto stabilito dalla Policy per l'accesso aperto dell'Università degli Studi di Firenze (https://www.sba.unifi.it/upload/policy-oa-2016-1.pdf)

Publisher copyright claim:

Conformità alle politiche dell'editore / Compliance to publisher's policies

Questa versione della pubblicazione è conforme a quanto richiesto dalle politiche dell'editore in materia di copyright.

This version of the publication conforms to the publisher's copyright policies.

(Article begins on next page)

23 January 2025

This article has been accepted for inclusion in a future issue of this journal. Content is final as presented, with the exception of pagination.

ArcSAR: Theory, Simulations, and Experimental Verification

Massimiliano Pieraccini, *Member, IEEE*, and Lapo Miccinesi

***Abstract*— ArcSAR is a ground-based synthetic aperture radar (GBSAR) that has recently been receiving increasing interest in the scientific literature. While the conventional GBSAR exploits the movement of an antenna along a linear rail to synthesize a large aperture, an ArcSAR exploits the spatial diversity of the data acquired by an antenna fixed to a rotating arm. The great advantage of ArcSAR is its capability to synthesize images at 360° with a constant resolution in azimuth. In this paper, the authors propose and test a new focusing algorithm that does not require to operate in the far field and neither with narrow beam antennas; moreover, it is flexible enough to focus on any plane (not necessarily on the rotation plane) as well as in the whole 3-D space. Furthermore, the authors demonstrate theoretically and experimentally that ArcSAR images can be affected by a "defocusing effect" of the targets far from the rotation plane, which has to be taken into consideration when designing such radars.**

***Index Terms*— Ground-based synthetic aperture radar (GBSAR), radar, remote sensing, synthetic aperture radar (SAR).**

I. Introduction

GROUND-BASED interferometric synthetic aperture radar (SAR) systems are popular remote sensing instruments able to provide radar images and detect small displacements at a great distance [1], [2]. The scientific literature reports a large number of applications: landslide monitoring [3], [4], glacier monitoring [5], open pit monitoring [6], bridges [7]–[9], and buildings [10] testing. The most common implementation of this kind of a radar is based on a linear mechanical guide (usually named "rail"). A radar head moving step-by-step on the guide is able to synthesize a radar aperture equivalent to twice the physical length of the rail [11]. This geometry is directly inspired by airborne or satellite SAR for which the trajectory can be locally considered linear [12]. Klausing [13] was the first to propose a SAR able to exploit the rotatory movement of the blades of a helicopter to synthesize a large aperture. He named it ROSAR. Jeon and Kim [14] developed a focusing algorithm able to take into account the migration. Bara *et al.* [15] proposed a fast algorithm. More recently, Lee *et al.* [16] tested an ArcSAR system set on a truck. Luo *et al.* [17] tested a less bulky equipment to detect changes on a slope and Ali *et al.* [18] designed a navigation radar for robot based on the ArcSAR, able to exploit both the rotational movement of an omnidirectional antenna and the linear translation of the robot.

In the opinion of the authors of this paper, the great advantage of the ground-based ArcSAR, with respect to conventional ground-based linear SAR, is the capability to obtain radar images at 360° with a constant angular resolution. This could be a very attractive feature to monitor large slopes or open pits [19]. Hence, the aim of this paper is a theoretical and experimental assessment of this radar technique.

Manuscript received June 10, 2016; revised September 13, 2016; accepted September 19, 2016.

The authors are with the Department of Information Engineering, University of Florence, 50138 Florence, Italy (e-mail: massimiliano.pieraccini@unifi.it).

Color versions of one or more of the figures in this paper are available online at http://ieeexplore.ieee.org.

Digital Object Identifier 10.1109/TMTT.2016.2613926

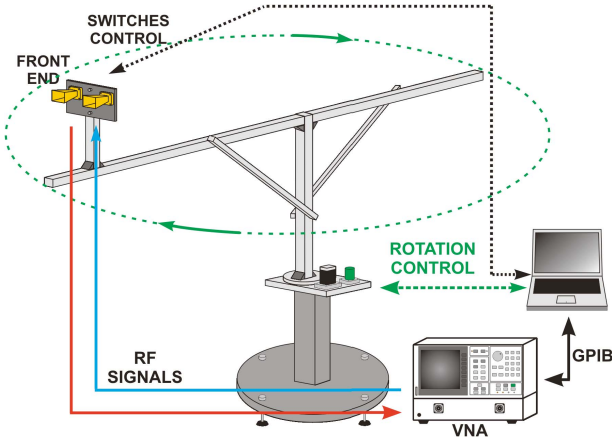

Fig. 1. ArcSAR prototype.

II. ArcSAR Prototype

The ArcSAR prototype we have assembled for testing the ArcSAR principle is shown in Fig. 1. It is a modified version of a radar already used in [20]–[22] for the proof of concept on another radar configuration: the RotoSAR.

A couple of antennas have been fixed on a rotating arm controlled by a step motor. The distance between the center of rotation and the median point of the centers of phase of antennas is $r_0 = 1.15$ m. A vector network analyzer (VNA) HP8720D operates as transceiver providing a continuous wave stepped frequency signal (CWSF) in X-band with central frequency $f_c = 10$ GHz and bandwidth $B = 200$ MHz. Two RF cables link the VNA to the frontend fixed at the rotating arm. The antennas are two horns whose details will be discussed in Section V.

With reference to Fig. 2, the VNA output power is 0 dBm, the one-way cable loss is -5 dB, and the TX amplifier gains 10 dB. Two single-pole double-throw switches provide a direct

0018-9480 © 2016 IEEE. Personal use is permitted, but republication/redistribution requires IEEE permission.
See http://www.ieee.org/publications_standards/publications/rights/index.html for more information.

This article has been accepted for inclusion in a future issue of this journal. Content is final as presented, with the exception of pagination.

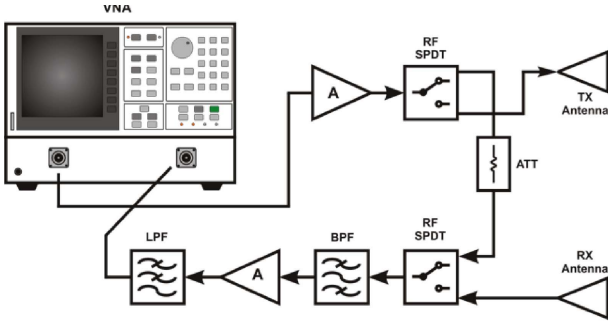

Fig. 2. Block scheme of radar.

path (through a 40 dB attenuator) between the transmitter and the receiver in order to perform calibrated measurements. The aim of the calibration is to avoid the movements of the cables from affecting the phase measurement. The gain of the RX amplifier is 20 dB.

The prototype operates step-by-step both in frequency and rotation. The number of frequencies N_f and the number of angular steps N_p in the circle have been set for avoiding range and angular ambiguity in the radar image. The unambiguous range R_u is given as [7]

$$R_u = \frac{c}{2B}(N_f - 1) \tag{1}$$

with c as the speed of light. Therefore, setting $N_f = 401$ results in $R_u = 300$ m, which is a reasonable value for the scenario where the prototype has been used.

The unambiguous azimuth φ_u is given as [7]

$$\frac{2\pi r_0}{N_p} \sin\left(\frac{\varphi_u}{2}\right) = \frac{\lambda}{4}. \tag{2}$$

For an omnidirectional antenna, φ_u should be 2π, but for a directional antenna, it is sufficient for φ_u to be considerably larger than the angular aperture of the antenna. As described in detail in Section V, the full-width at half-maximum (FWHM) of the pattern of the horn antenna we used is 20.88°. Therefore, considering a margin factor of 3, we have set $N_p = 500$.

III. Focusing Algorithm

The basic idea of the ArcSAR is to synthesize a large aperture exploiting the spatial diversity of data acquired by an antenna fixed to a horizontally rotating arm. Several algorithms have been proposed in [13]–[16]. The tradeoff of all these methods is between the accuracy and computational weight: algorithms that do not make approximations are too slow to be applied in operating radars; on the other hand, any approximation limits the field of applicability. Some approximated SAR formulations rely on the supposition of narrow beam antenna [16], but this can be a very strict limitation for exploiting the full resolution potential of ArcSAR. The novel algorithm we propose in this paper is able to operate in the near field as well as in the far field, it is not limited to narrow beam antennas, and it is flexible enough to focus on any plane (not necessarily the rotation plane) as well as in the whole 3-D space.

Generally speaking, an ArcSAR (also named ROSAR [13] or C-SAR [15]) is a system acquiring SAR images from the 360° (or a smaller angle) surrounding environment with an antenna fixed to a rotating arm. In the case of a system, operating step-by-step both in the frequency (CWSF) and rotation angle the result of a measurement is a matrix $N_f \times N_p$ of complex numbers

$$E_{i,k} = I_{i,k} + j\,Q_{i,k} \tag{3}$$

where $I_{i,k}$ and $Q_{i,k}$ are the in-phase and the quadrature components acquired at ith frequency ($1 < i < N_f$) in the kth position ($1 < k < N_p$). The basic formula for focusing on a generic point (x, y, z) of the space surrounding the radar is [7]–[22]

$$I(x, y, z) = \sum_{i,k} E_{i,k} e^{j\frac{4\pi}{c} f_i R_k} \tag{4}$$

where R_k is the distance between the (x, y, z) image point and the kth position on the antenna on the circle. Equation (4) is computationally heavy, so the key point of any focusing algorithm is to reduce its computational cost without a significant loss of generality and accuracy. The first step in the algorithm we propose is to focus the matrix E_{ik} in range (i.e., along the i-index). A suitable window has to be applied to measured data for lowering the sidelobes (in particular we used a Kaiser window with $\beta = 5$ that gives sidelobes in range lower then -40 dB), aftermath the matrix E_{ik} has to be zero-padded of a factor F (it means that each column will have FN_f elements of which the last $(F-1)N_f$ zeroes). Finally, the matrix is focused in range as follows:

$$u(n, k) = \frac{1}{FN_f} \sum_{i=1}^{i=FN_f} E_{i,k} e^{j\frac{4\pi}{c}(f_1 + (i-1)\Delta f)(n-1)\Delta R} \tag{5}$$

where f_1 is the first frequency of the bandwidth $B = f_{N_f} - f_1$, Δf is the frequency step, and ΔR is the range step.

By imposing

$$\Delta R = \frac{c}{2N_f F \Delta f} = \frac{N_f - 1}{N_f F}\frac{c}{2B} \tag{6}$$

(5) becomes

$$\begin{aligned} u(n, k) &= e^{j\frac{4\pi}{c} f_1 (n-1)\Delta R} \frac{1}{FN_f} \sum_{i=1}^{i=FN_f} E_{i,k} e^{j\frac{2\pi}{N_f}(i-1)(n-1)} \\ &= e^{j\frac{4\pi}{c} f_1 (n-1)\Delta R} \mathrm{IFFT}_i(E_{i,k}, FN_f) \end{aligned} \tag{7}$$

where $\mathrm{IFFT}_i(E_{i,k}, FN_f)$ is the inverse fast Fourier transform of $E_{i,k}$ with a padding factor F.

With reference to Fig. 3, the focused image in a generic point (x, y, z) is given as

$$I(x, y, z) = \sum_k u(n(x, y, z, k), k) \tag{8}$$

with

$$n(x, y, z, k) = \mathrm{integer}\left(\frac{R(x, y, z, k)}{\Delta R}\right). \tag{9}$$

This article has been accepted for inclusion in a future issue of this journal. Content is final as presented, with the exception of pagination.

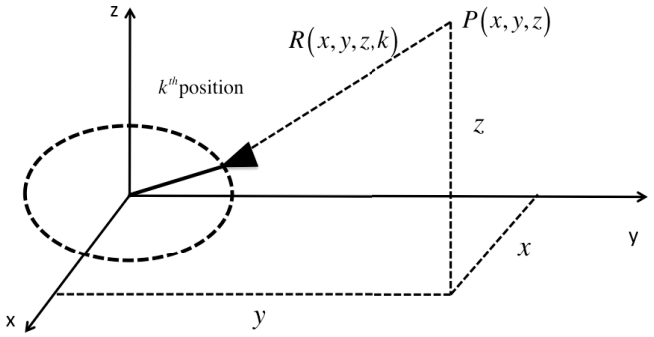

Fig. 3. Geometry of ArcSAR focusing algorithm.

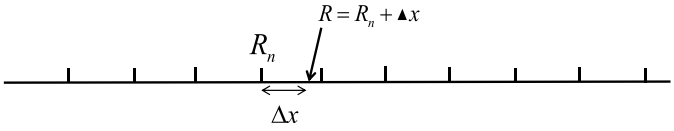

Fig. 4. Interpolation in range.

Obviously, if the antenna is not omnidirective, the summation has to be limited to the k-indices where the antenna sees the image point $P(x, y, z)$.

The critical point of this approach is that the fractional part discharged in (8) must be negligible with respect of the wavelength ($\lambda = c/f_c$ with f_c central frequency). This means that ΔR should be $\ll\lambda$, and therefore the padding factor (F) should be

$$F \gg \frac{1}{\lambda}\frac{c}{2B}. \tag{10}$$

In the practical case, F could be of the order of several hundreds and this can give impractical matrices to manage to nullify the computational advantage of IFFT.

For this reason, it is convenient to implement an interpolation procedure as follows.

With reference to Fig. 4, the range focusing of the $E_{i,k}$ matrix at range R is

$$u(R,k) = \frac{1}{FN_f}\sum_{i=1}^{i=FN_f} E_{i,k}e^{j\frac{4\pi}{c}(f_1+(i-1)\Delta f)(R+\Delta x)} \tag{11}$$

which, for $B/f_c \ll 1$, becomes

$$u(R,k) = e^{j\frac{4\pi}{c}f_1 R}\mathrm{IFFT}_i(E_{i,k}, FN_f)e^{j\frac{4\pi}{c}\frac{B}{2}(R-(n-1)\Delta R)} \tag{12}$$

or with a further approximation

$$u(R,k) = e^{j\frac{4\pi}{c}f_1 R}\mathrm{IFFT}_i(E_{i,k}, FN_f). \tag{13}$$

In order to evaluate the performances of the algorithm in a simulated (but realistic) case, we consider a target at a 50 m distance as $f_c = 10$ GHz, $B = 200$ MHz, $N_f = 401$, and $F = 10$. Fig. 5 shows the amplitude of the peak in range at $R = 50$ m. The trace in blue is calculated without approximations using (4), while traces (A), (B), and (C) are relative, respectively, to (8), (13), and (12). The three traces are perfectly overlapping.

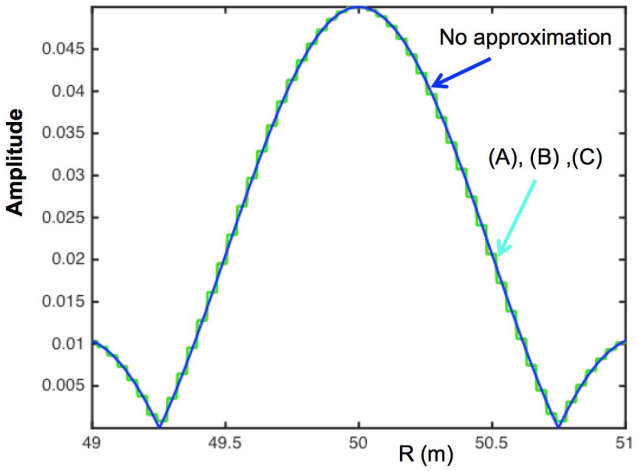

Fig. 5. Amplitude in range using algorithms (A), (B), and (C).

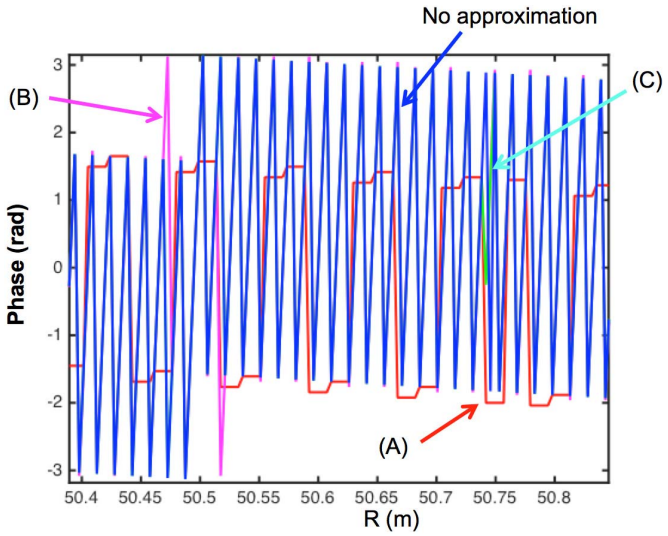

Fig. 6. Phase in range using algorithms (A), (B), and (C).

Although in amplitude the three algorithms (A), (B), and (C) are equivalent, their performances on phase are dramatically different. Fig. 6 shows the calculated phase. It is evident that algorithm (A) is surely unsatisfactory as it loses the phase waveform completely; algorithm (B) appears more satisfactory, but sometimes gives notable errors; (C) is the best with very small phase errors.

In order to evaluate the impact of the phase error in the focused complex image, we calculated the modulus of the difference (in the complex numbers domain) between (A), (B), and (C) and the trace calculated without approximation using (4). The plots shown in Fig. 7 confirm that (A) results unsatisfactory, (B) looks satisfactory, but (C) is the best.

These results obviously depend on the padding factor F. As it increases, all the algorithms should improve their performances. In order to confirm and quantify this statement, we calculated the maximum error (in the whole range) of the three algorithms by varying the padding factor. The results are shown in Fig. 8.

We can conclude as expected that all the algorithms converge to the right value increasing F, but

This article has been accepted for inclusion in a future issue of this journal. Content is final as presented, with the exception of pagination.

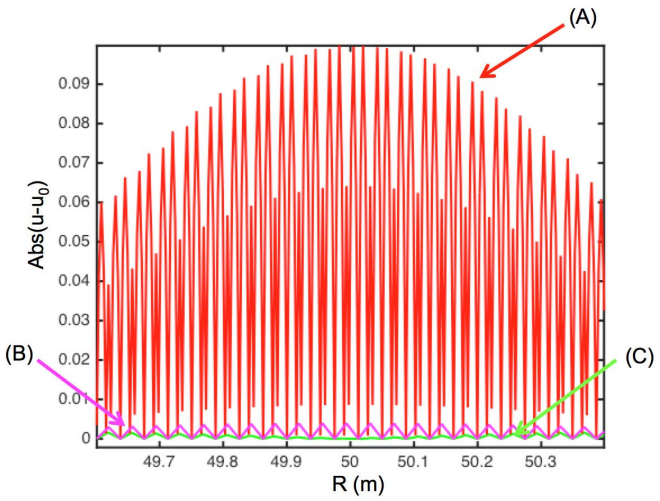

Fig. 7. Modulus of the error in range (calculated as difference between complex numbers) using algorithms (A), (B), and (C).

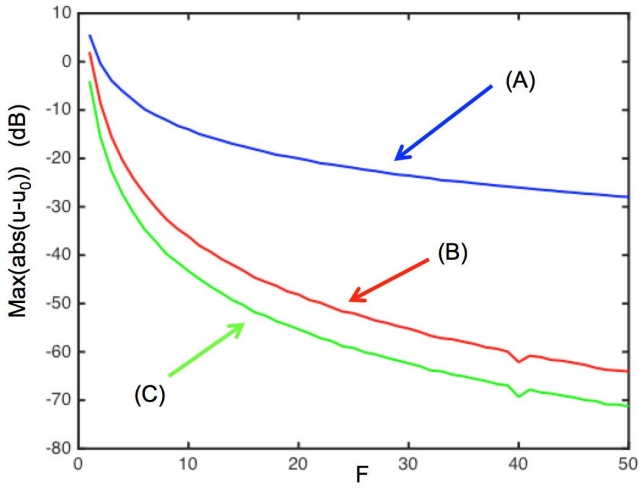

Fig. 8. Maximum error of algorithms (A), (B), and (C), varying the padding factor F.

algorithms (B) and (C) converge much faster. For example for $F = 25$, (B) is about 30 dB better than (A), and (C) is about further 10 dB better.

IV. Azimuth Resolution

A great advantage of the ground-based ArcSAR, with respect to the conventional ground-based linear SAR, is its capability to obtain radar images at 360° with a constant angular resolution. This is an obvious consequence of the circular symmetry of the geometry.

With reference to Fig. 9, if φ_0 is the angular aperture of the antenna, the portion of the arc that contributes to the synthesis of the image at point P is AB.

On the other hand, the azimuth resolution ($\Delta\varphi$) of the SAR image depends on the linear length d of the chord of arc as seen from the image point, trough the following equation [11]:

$$d \sin\left(\frac{\Delta\varphi}{2}\right) = \frac{\lambda}{4}. \tag{14}$$

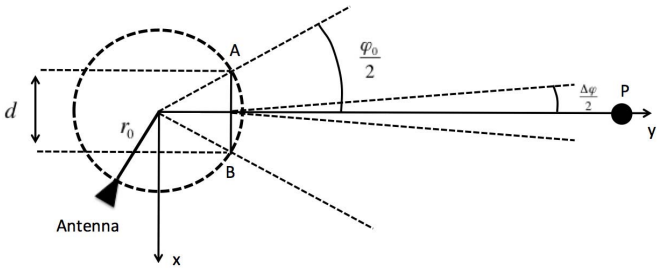

Fig. 9. Geometry of ArcSAR in xy plane.

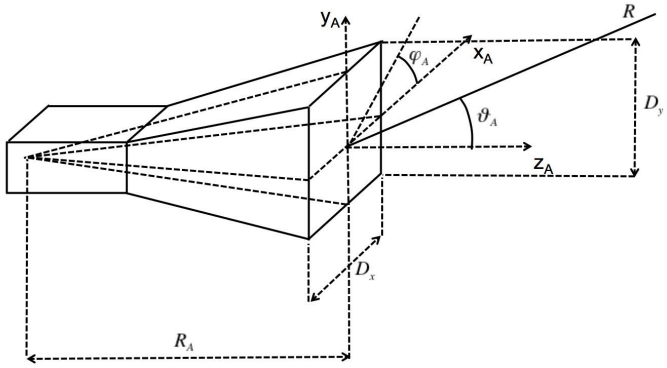

Fig. 10. Horn antenna.

From Fig. 9, d is given as

$$d = 2r_0 \sin\left(\frac{\varphi_0}{2}\right). \tag{15}$$

The angular aperture of the physical antenna is given as [11]

$$D_x \sin\left(\frac{\varphi_0}{2}\right) = \frac{\lambda}{2} \tag{16}$$

with D_x width of the antenna. Substituting (15) and (16) into (14) we obtain the notable equation

$$\sin\left(\frac{\Delta\varphi}{2}\right) = \frac{D_x}{4r_0} \tag{17}$$

where the azimuth resolution depends only on the antenna width and on the radius of ArcSAR. Obviously, (17) is just a rough evaluation of the azimuth resolution. For a more accurate assessment, it is necessary to model the antenna pattern.

V. Antenna Modeling

As seen before, the azimuth resolution on an ArcSAR depends on the antenna pattern [contrary to linear ground-based SAR (GBSAR)]. Hence, for a realistic evaluation of the performances of an ArcSAR, a suitable antenna model is necessary.

The ArcSAR prototype we assembled makes use of horn antennas linearly polarized in the y-direction. With reference to Fig. 10 their radiated pattern can be calculated as follows

This article has been accepted for inclusion in a future issue of this journal. Content is final as presented, with the exception of pagination.

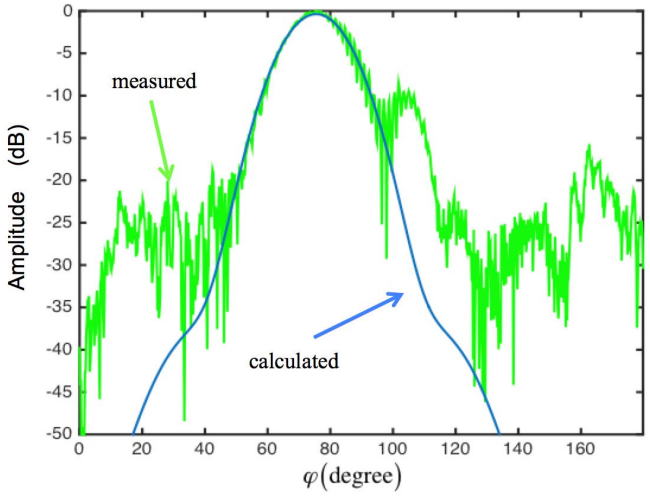

Fig. 11. Antenna lobe.

[23]:

$$P(\vartheta_A, \varphi_A) = \frac{1}{2\lambda}(1+\cos\vartheta_A) \times \int_{x_A=-\frac{D_x}{2}}^{x_A=\frac{D_x}{2}} \int_{y_A=-\frac{D_y}{2}}^{y_A=\frac{D_y}{2}} \times E_A(x_A, y_A) e^{j\frac{2\pi}{c} f_c (x_A \sin\vartheta_A \cos\varphi_A + y_A \sin\vartheta_A \sin\varphi_A)} dx_A dy_A \quad (18)$$

with

$$E_A(x_A, y_A) = E_0 \cos\left(\frac{\pi x_A}{D_x}\right) e^{-\frac{2\pi}{c} f_c \left(\frac{x_A^2}{R_A} + \frac{x_B^2}{R_A}\right)}. \quad (19)$$

The angles θ_A and φ_A define the direction of the electromagnetic wave with respect to the reference system fixed by the x_A-axis, y_A-axis, and z_A-axis; D_x and D_y are the physical sizes of the horn mouth; R_A is the distance between the horn mouth and the phase center; and f_c is the central frequency.

In order to evaluate the agreement between the mathematical model and the antennas we used, a corner reflector (CR) of side 0.4 m × 0.4 m has been put on the plane of rotation of the ArcSAR at a distance of 22 m. The angle φ_{CR} between the x-axis of ArcSAR and the CR direction was 75°. By rotating the arm it has been possible to measure the amplitude of the pattern to be compared with the calculated one. Note that in this geometric arrangement, $\varphi_A = 0$ and $\vartheta_A = \varphi - \varphi_{CR}$. The physical dimensions of the horn were $D_x = 75$ mm, $D_y = 50$ mm, and $R_A = 125$ mm. The obtained results are shown in Fig. 11. The two traces have been normalized to their maximum. The FWHA of the main peak is 20.88°. The small peak on the right side is due to the residual of a target at a larger distance. By considering that this measurement has not been performed in an anechoic chamber, the agreement between the measured and calculated traces appears surely satisfactory for our purposes.

VI. Experimental Evaluation of Azimuth Resolution

The experimental arrangement for the measurement of the antenna pattern can also be used for experimentally validating the theory and the focusing algorithm described before. The obtained range-focused image is shown in Fig. 12. The CR is well evident.

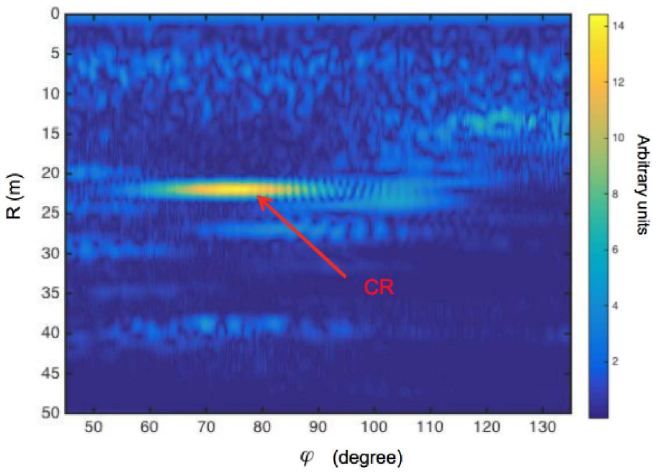

Fig. 12. Range focused image.

By focusing on the (x, y) plane using (8) with the approximation (C), we obtained the amplitude image in Fig. 13.

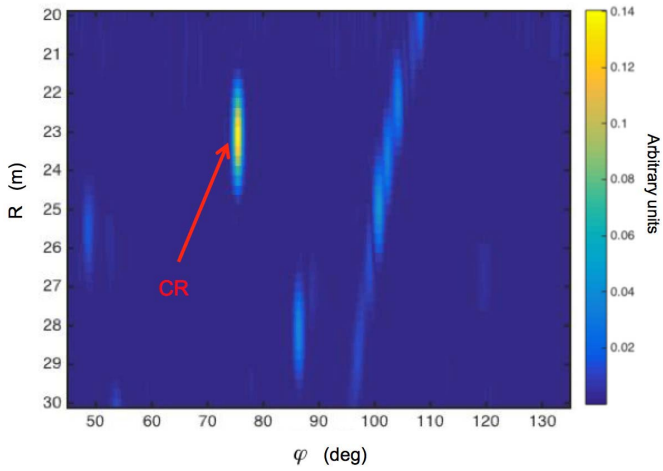

Fig. 13. Range and azimuth focused image.

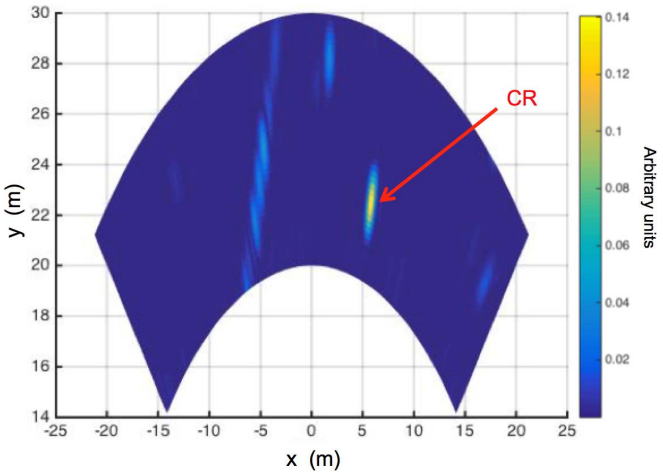

Fig. 14. Focused image in Cartesian coordinates.

This article has been accepted for inclusion in a future issue of this journal. Content is final as presented, with the exception of pagination.

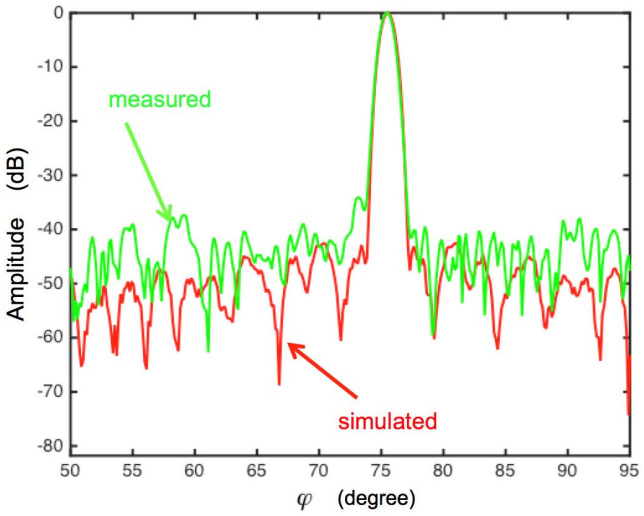

Fig. 15. Simulated and measured PSFs in azimuth of a CR at range $R = 22$ m.

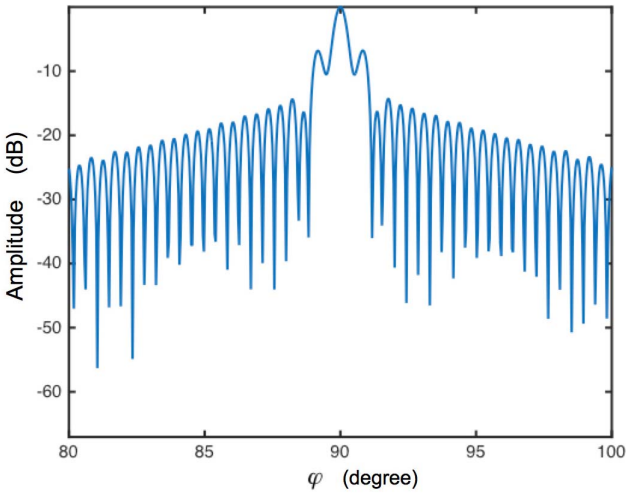

Fig. 16. Simulated PSF for $D_x = 10$ mm.

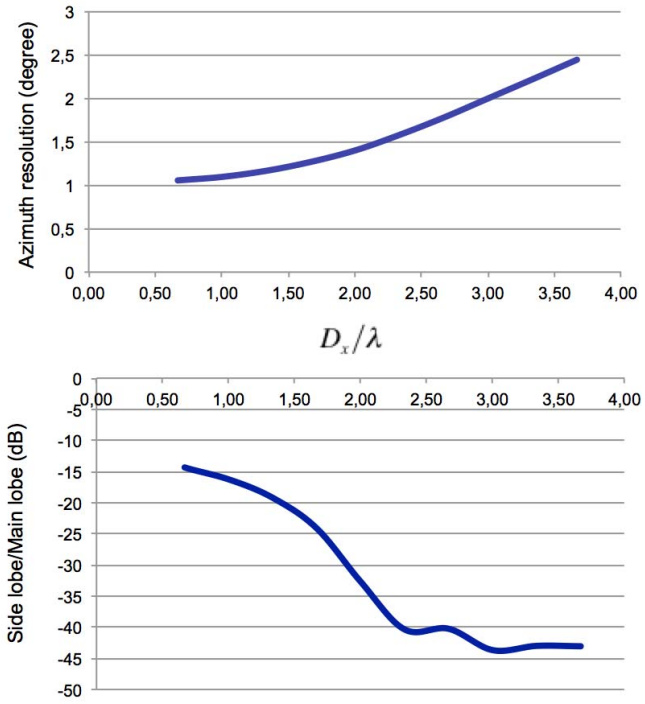

Fig. 17. Azimuth resolution and side lobes amplitude.

The image in Fig. 13 can also be represented in Cartesian coordinates as shown in Fig. 14.

Finally, Fig. 15 shows the direct comparison of the measured and simulated peaks at the range of the CR, i.e., the measured and simulated point spread functions (PSFs) in azimuth. The agreement is very satisfactory.

The FWHM of the peak (measured and simulated) is 1.39°. The angular resolution roughly estimated with (17) was 1.87°.

VII. Tradeoff Between Azimuth Resolution and Sidelobes

Generally speaking, the wider the antenna pattern the better the azimuth resolution. An omnidirectional antenna can synthesize an aperture equal to the diameter, i.e., the largest possible aperture. Unfortunately, the wider the antenna pattern the higher the side lobes in the focused image. As an extreme case, the PSF of an omnidirectional antenna that rotates for 360° is the Bessel function [13], with side lobes at −6 dB with respect to the main lobe. Images affected by such side lobes are unusable in most applications.

By limiting the analysis to the horn antennas, we have simulated the PSF for a target at 10 m using the following parameters: $f_c = 10$ GHz, $B = 200$ MHz, $D_y = 50$ mm, $R_A = 112$ mm, and varying D_x. For example, for $D_x = 10$ mm the simulated PSF is shown in Fig. 16.

Fig. 17 shows the plot of the azimuth resolution versus the width of antenna (D_x) and the calculated ratio between the side lobes and the main lobe.

The plot appears to show a simple rule-of-thumb: when the width of antenna is about twice the wavelength the side lobes do not lower significantly further.

VIII. "Defocusing" Effect

A peculiar characteristic of ArcSAR (that does not have a linear SAR) is providing a resolution also in elevation for image points with $z \neq 0$. Indeed, as shown in Fig. 18, the antenna movement has a component along the y-axis (the segment Δr_0), which in turn has a projection (Δd) in the plane that is orthogonal to the view direction.

Unfortunately, this resolution is not high enough to be exploited to synthesize 3-D imaging but it could be enough to give an annoying "defocusing effect" when an image is focused on the rotation plane.

The experimental setup shown in Fig. 19 has been arranged in order to experimentally verify this effect.

The CR was positioned on the tip of a wood beam. Its height with respect to the rotation plane was 3.5 m. The distance between the radar and the base of the beam was 11.61 m. In this configuration the ArcSAR should have an angular resolution also in elevation (θ), in order to verify that the focusing algorithm has been applied on the vertical plane

This article has been accepted for inclusion in a future issue of this journal. Content is final as presented, with the exception of pagination.

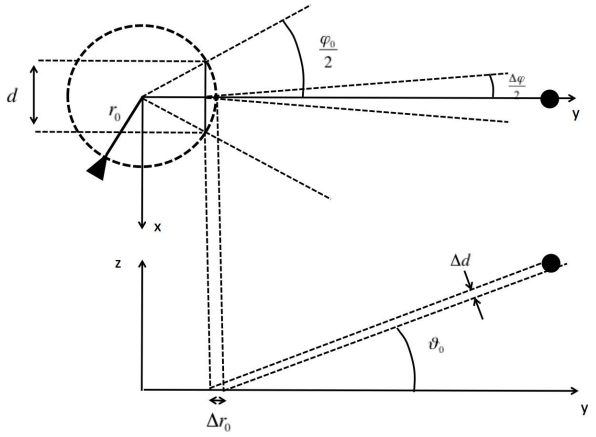

Fig. 18. Geometry of ArcSAR in *xy* and *yz* planes.

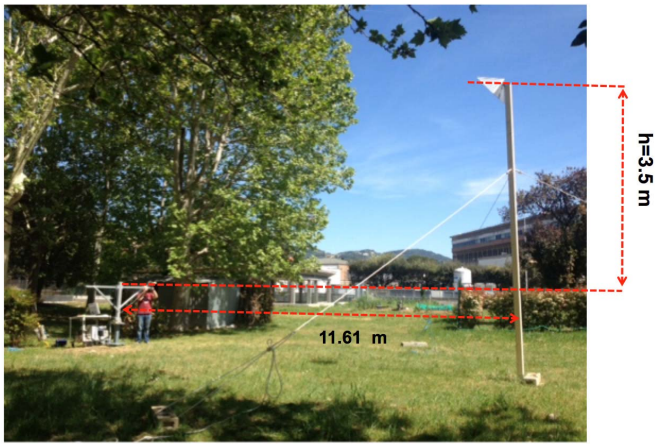

Fig. 19. Measurement setup.

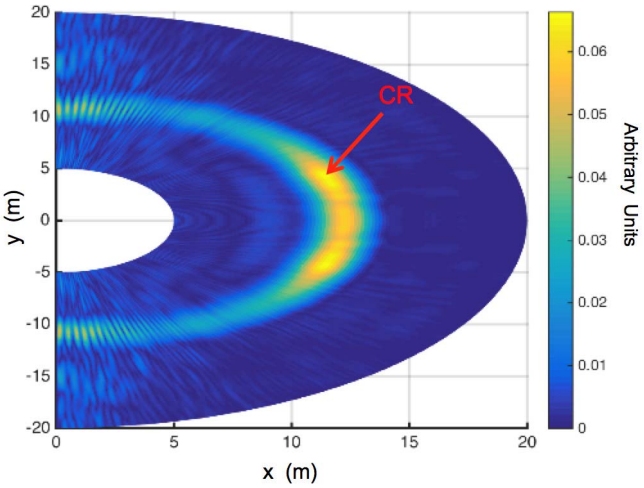

Fig. 20. Image focused in the *yz* plane.

yz that crosses the rotation center of the radar and the CR. The obtained image is shown in Fig. 20

Fig. 21 shows the plot of the PSF in elevation at $R = 12.1$ m. The green line is the image focused using the experimental data while the red line is the simulated image.

It is interesting to note the image is symmetric with respect to the plane *xy*. This is a consequence of the symmetry of the radar geometry that does not allow to discriminate between

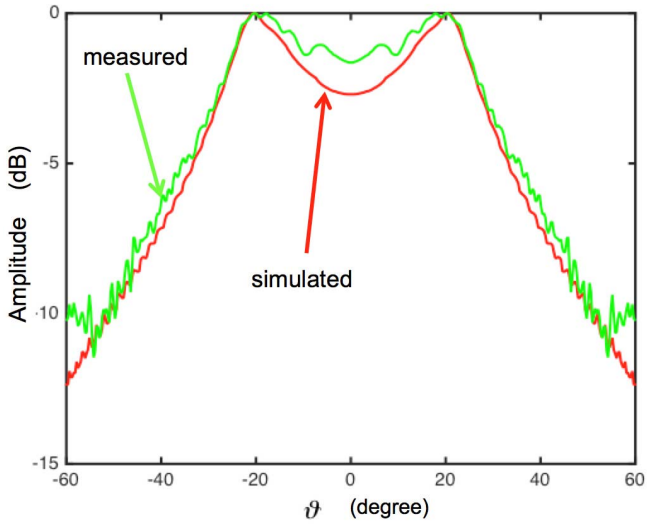

Fig. 21. PSF in elevation at $R = 12.1$ m.

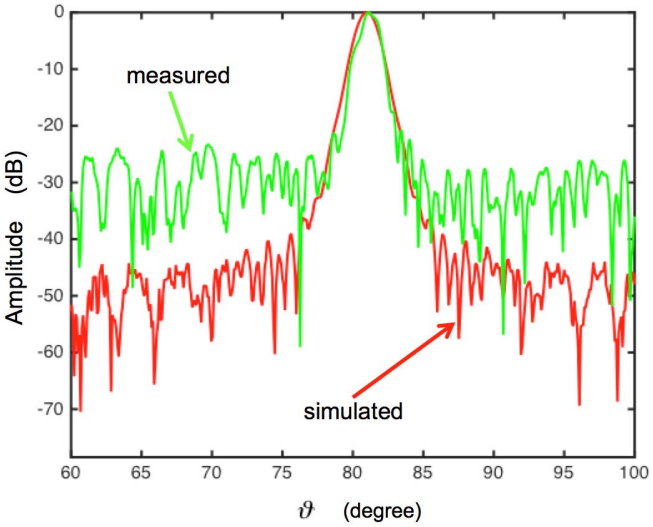

Fig. 22. Azimuth resolution of a target far from the *xy* plane.

up and down. Fig. 21 clearly shows that ArcSAR has a resolution (although low) in elevation. As a consequence, when a target far from the *xy* plane is focused in the *xy* plane, its resolution is degraded. This can be seen directly from Fig. 22 where the simulated and measured plots of PSF in azimuth at $R = 12.1$ m is shown. The angular resolution results in 2.12° , sensibly larger than 1.39° obtained for a target in the *xy* plane.

Considering the good agreement between the measured and simulated plots, the only simulation can be effectively used for assessing the degradation of resolution. The plot in Fig. 23 shows the increase in the azimuth resolution with the elevation of the target. The plot has been obtained through simulation.

IX. 360° Radar Imaging and Interferometry

In order to verify the unique capability of ArcSAR to obtain 360° images, the radar has been positioned in a garden as shown in Fig. 24. The height of the antennas from the soil was 1.62 m.

This article has been accepted for inclusion in a future issue of this journal. Content is final as presented, with the exception of pagination.

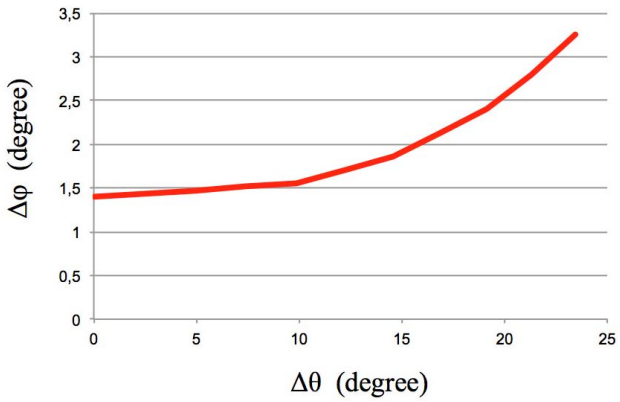

Fig. 23. Azimuth resolution in function of the target elevation.

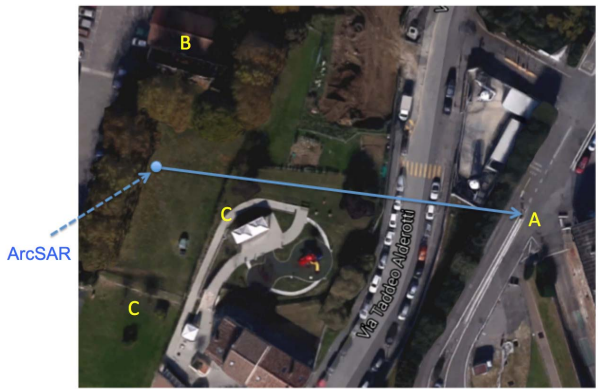

Fig. 24. Measurement scenario.

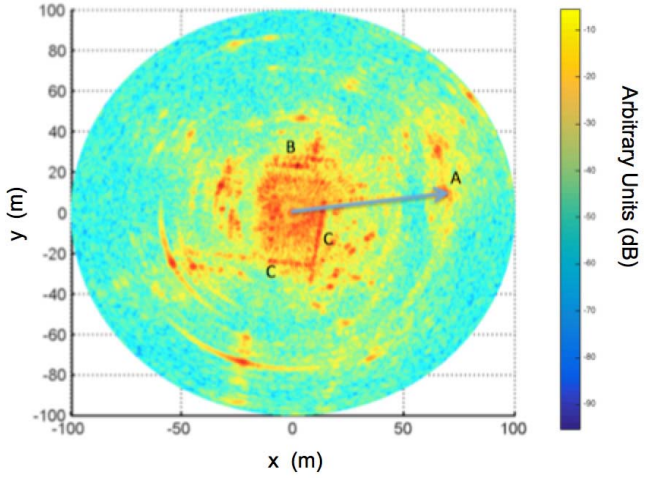

Fig. 25. Radar image of the scenario in Fig. 24.

The acquired data has been focused with method (B) and the obtained radar image (in logarithmic scale) is shown in Fig. 25.

There are features well evident: the pylon (A), the wall and the roof of a two-story building in masonry (B), and the metallic fence (C).

As the GBSAR is often used for detecting small displacements at a distance through differential interferometry [1], [2] we also verified experimentally this capability of ArcSAR.

Fig. 26. Differential interferometry with a micrometric positioner.

With this aim, a CR was fixed on a holder able to provide calibrated displacements along the range direction with an accuracy of 0.1 mm (the micrometric positioner shown in Fig. 26). It was positioned at a 15 m distance from the radar and two measurements were performed before and after a nominal displacement of 4.0 mm. The experimentally detected displacement was 4.01 mm, in complete agreement with the nominal value

X. Conclusion

A focusing algorithm for ArcSAR has been proposed and tested with experimental data. As its working principle is based on the compensation of the phase history of each path between the measurement points and the image point, the ArcSAR focusing algorithm does not require to operate in far field and neither with narrow beam antennas; moreover, it is flexible enough to focus on any plane (not necessarily on the rotation plane) as well as in the whole 3-D space.

Furthermore, it has been identified a possible problem of ArcSAR consisting in the "defocusing" of targets far from the rotation plane. Since this problem is due to the resolution in elevation of the ArcSAR, it can be solved by just focusing on the effective 3-D shape, i.e., the digital elevation model (DEM) of the scenario where the radar is operated. In addition, the proposed algorithm can be used to focus on the DEM as it does not make assumptions on the shape of the focalization surface.

References

[1] O. Monserrat, M. Crosetto, and G. Luzi, "A review of ground-based SAR interferometry for deformation measurement," *ISPRS J. Photogram. Remote Sens.*, vol. 93, pp. 40–48, Jul. 2014.

[2] M. Pieraccini, "Monitoring of civil infrastructures by interferometric radar: A review," *Sci. World J.*, vol. 2013, 2013, Art. no. 786961.

[3] M. Pieraccini *et al.*, "Landslide monitoring by ground-based radar interferometry: A field test in Valdarno (Italy)," *Int. J. Remote Sens.*, vol. 24, no. 6, pp. 1385–1391, 2003.

[4] G. Antonello *et al.*, "Ground-based SAR interferometry for monitoring mass movements," *Landslides*, vol. 1, no. 1, pp. 21–28, Mar. 2004.

[5] L. Noferini, D. Mecatti, G. Macaluso, M. Pieraccini, and C. Atzeni, "Monitoring of Belvedere Glacier using a wide angle GB-SAR interferometer," *J. Appl. Geophys.*, vol. 68, no. 2, pp. 289–293, Jun. 2009.

This article has been accepted for inclusion in a future issue of this journal. Content is final as presented, with the exception of pagination.

[6] D. Mecatti, G. Macaluso, A. Barucci, L. Noferini, M. Pieraccini, and C. Atzeni, "Monitoring open-pit quarries by interferometric radar for safety purposes," in *Proc. Eur. Radar Conf. (EuRAD)*, vol. 30. Sep./Oct. 2010, pp. 37–40.
[7] M. Pieraccini *et al.*, "Structural static testing by interferometric synthetic radar," *NDT E Int.*, vol. 33, no. 8, pp. 565–570, Dec. 2000.
[8] D. Dei, M. Pieraccini, M. Fratini, C. Atzeni, and G. Bartoli, "Detection of vertical bending and torsional movements of a bridge using a coherent radar," *NDT E Int.*, vol. 42, no. 8, pp. 741–747, Dec. 2009.
[9] D. Dei, D. Mecatti, and M. Pieraccini, "Static testing of a bridge using an interferometric radar: The case study of 'ponte degli alpini,' Belluno, Italy," *Sci. World J.*, vol. 2013, 2013, Art. no. 504958.
[10] M. Pieraccini *et al.*, "Remote sensing of building structural displacements using a microwave interferometer with imaging capability," *NDT E Int.*, vol. 37, no. 7, pp. 545–550, Oct. 2004.
[11] M. Pieraccini, "Real Beam vs. Synthetic aperture radar for slope monitoring," in *Proc. Prog. Electromagn. Res. Symp. (PIERS)*, Stockholm, Sweden, Aug. 2013, pp. 1627–1630.
[12] G. Fornaro, G. Franceschetti, and S. Perna, "Motion compensation errors: Effects on the accuracy of airborne SAR images," *IEEE Trans. Aerosp. Electron. Syst.*, vol. 41, no. 4, pp. 1338–1352, Oct. 2005.
[13] H. Klausing, "Feasibility of a synthetic aperture radar with rotating antennas (ROSAR)," in *Proc. 9th Eur. Microw. Conf.*, Sep. 1989, pp. 287–299.
[14] M. Jeon and Y. S. Kim, "Migration technique for rotor synthetic aperture radar," *Electron. Lett.*, vol. 33, no. 7, pp. 630–631, Mar. 1997.
[15] M. Bara, L. Sagués, F. Paniagua, A. Broquetas, and X. Fàbregas, "High-speed focusing algorithm for circular synthetic aperture radar (C-SAR)," *Electron. Lett.*, vol. 36, no. 9, pp. 1–2, Apr. 2000.
[16] H. Lee, J.-H. Lee, K.-E. Kim, N.-H. Sung, and S.-J. Cho, "Development of a truck-mounted arc-scanning synthetic aperture radar," *IEEE Trans. Geosci. Remote Sens.*, vol. 52, no. 5, pp. 2773–2779, May 2014.
[17] Y. Luo, H. Song, R. Wang, Y. Deng, F. Zhao, and Z. Xu, "Arc FMCW SAR and applications in ground monitoring," *IEEE Trans. Geosci. Remote Sens.*, vol. 52, no. 9, pp. 5989–5998, Sep. 2014.
[18] F. Ali, G. Bauer, and M. Vossiek, "A rotating synthetic aperture radar imaging concept for robot navigation," *IEEE Trans. Microw. Theory Techn.*, vol. 62, no. 7, pp. 1545–1553, Jul. 2014.
[19] C. Atzeni, M. Barla, M. Pieraccini, and F. Antolini, "Early warning monitoring of natural and engineered slopes with ground-based synthetic-aperture radar," *Rock Mech. Rock Eng.*, vol. 48, no. 1, pp. 235–246, 2015.
[20] M. Pieraccini, F. Papi, and S. Rocchio, "Interferometric rotoSAR," *Electron. Lett.*, vol. 51, no. 18, pp. 1451–1453, Sep. 2015.
[21] M. Pieraccini, N. Agostini, F. Papi, and S. Rocchio, "A rotating antenna ground-based SAR," in *Proc. IEEE Eur. Microw. Conf. (EuMC)*, Sep. 2015, pp. 1515–1518.
[22] M. Pieraccini, F. Papi, and S. Rocchio, "SAR imagery by roto-SAR," in *Proc. IEEE Int. Conf. Microw., Commun., Antennas Electron. Syst. (COMCAS)*, Nov. 2015, pp. 1–5.
[23] C. A. Balanis, *Antenna Theory: Analysis and Design*, 3rd ed. Hoboken, NJ, USA: Wiley, 2005.

Massimiliano Pieraccini (M'13) received the M.S. degree in physics and the Ph.D. degree in non-destructive testing from the University of Florence, Florence, Italy, in 1994 and 1998, respectively.

In 1995, he joined the Department of Electronics and Telecommunications, University of Florence, where he was an Assistant Professor in 1997. Since 2005, he has been an Associate Professor. His previous research interests included optoelectronic sensors, ultrasound transducers, 3-D acquisition systems, interferometric radar, and ground penetrating radar.

Mr. Pieraccini was the Technical Chair of the 13th International Conference on Ground Penetrating Radar in 2010 and the General Chair of the 7th International Workshop on Advanced Ground Penetrating Radar Symposium in Ground Penetrating Radar in 2015. He was a recipient of the Nello Carrara Prize at the University of Florence.

Lapo Miccinesi was born in Florence, Italy, in 1988. He received the B.S. degree in physics and M.S. degree in physics of particles from the University of Florence, Florence, in 2011 and 2016, respectively.

He is currently with the Department of Information Engineering, University of Florence, as a Post-Degree Grant Recipient. His previous research interests included the detector of particles, acquisition systems, and ground based radar.